http://www.diva-portal.org

Preprint

This is the submitted version of a paper presented at *15th European Wave and Tidal Energy Conference, Bilbao, Spain, 3-7 September, 2023*.

Citation for the original published paper:

Fjellstedt, C., Forslund, J., Thomas, K. (2023)
A comparison of AC and DC collection grids for marine current energy
In: *Proceedings of the 15th European Wave and Tidal Energy Conference, Bilbao, 3-7 September 2023*, 207 European Wave and Tidal Energy Conference
Proceedings of the European Wave and Tidal Energy Conference (EWTEC)
https://doi.org/10.36688/ewtec-2023-207

N.B. When citing this work, cite the original published paper.

Permanent link to this version:
http://urn.kb.se/resolve?urn=urn:nbn:se:uu:diva-511633

A comparison of AC and DC collection grids for marine current energy

Christoffer Fjellstedt, Johan Forslund, and Karin Thomas

Abstract—**Important questions to enable the use of marine current energy are how the electrical system is designed, how multiple energy converters are interconnected offshore and how the power is transmitted to the shore. The Division of Electricity at Uppsala University have constructed and deployed a marine current energy converter in the river Dalälven in Söderfors, Sweden. In the study presented in this article, a model of a near-shore low-voltage AC collection grid and a near-shore low-voltage DC collection grid is presented for the technology at the Söderfors test site. The models are implemented in MATLAB/Simulink. For collection grids of five turbines, it is shown that the proposed control schemes are able to deliver power to the distribution grid. The controllers are able to achieve this even when one turbine is suddenly disconnected from the grid. Furthermore, it is shown that the conduction losses of the DC system are higher than the losses of the AC system for nominal and high water speeds. However, in a qualitative comparison between the systems it is concluded that despite the higher losses, the DC system can be an interesting option. This is because fewer components need to be placed in the turbine, which is beneficial in offshore systems where space is a limiting factor. Furthermore, a DC system can be less expensive since fewer cables are needed.**

Index Terms—**Marine current energy, AC collection grids, DC collection grids, Electrical systems**

I. INTRODUCTION

THE demand for renewable energy is growing. In order to achieve net zero emission from the energy sector globally by 2050, 825 GW of renewable energy need to be installed annually until 2050 [1]. Marine energy sources have the potential to contribute significantly to increasing the level of energy from renewable energy sources.

An important consideration to enable the use of more marine energy sources is how the energy source is connected to the electrical grid. Furthermore, it is necessary to consider how multiple energy converters are interconnected in an offshore farm and how the power is transmitted to the shore.

© 2023 European Wave and Tidal Energy Conference. This paper has been subjected to single-blind peer review.

This work was supported by STandUP for Energy

Christoffer Fjellstedt is with the Division of Electricity, Department of Electrical Engineering at Uppsala University, Ångströmlaboratoriet, Lägerhyddsvägen 1, 752 37 Uppsala, Sweden (e-mail: christoffer.fjellstedt@angstrom.uu.se).

Johan Forslund is with the Division of Electricity, Department of Electrical Engineering at Uppsala University, Ångströmlaboratoriet, Lägerhyddsvägen 1, 752 37 Uppsala, Sweden (e-mail: johan.forslund@angstrom.uu.se).

Karin Thomas is with the Division of Electricity, Department of Electrical Engineering at Uppsala University, Ångströmlaboratoriet, Lägerhyddsvägen 1, 752 37 Uppsala, Sweden (e-mail: karin.thomas@uu.se).

Digital Object Identifier:
https://doi.org/10.36688/ewtec-2023-207

A fairly limited amount of research has been conducted on how the electrical system for marine energy converters should be constructed, at least compared to the research within the offshore wind power sector. Especially research with the focus on power collection grids for multiple marine energy converters is lacking. In three reports from ORE Catapult a comprehensive review and technical assessment of possible electrical systems and array networks for marine energy converters can be found [2]–[4]. However, the content in the reports had a general perspective, and the emphasis was not on a specific technology or site-specific investigations, for example, the control of individual marine energy converters in an array. In [5] a techno-economical review of electrical components for marine energy arrays was given. The focus was on identifying the key components in the systems and discussing technical and cost considerations for the components. These types of studies give a good insight into how an offshore system can be constructed from a general perspective. However, the investigation of how the control system can be expected to behave for a specific case is still lacking. In this paper, a study concentrated on the operation of offshore power collection grids for a specific marine current energy converter will be presented.

A natural starting point for the development of the electrical system and offshore grid for marine energy sources is to investigate the current state of technology in offshore wind and apply the technologies and control methods to the specific conditions for marine energy sources. Offshore wind farms have mainly been constructed using AC collection grids [6], [7]. However, the transmission of power to the shore has been performed using HVDC. Regarding the layout of AC collection grids, many different topologies have been proposed in the literature [8]–[12]. A common topology is the radial topology, where the energy converters are connected to a radial feeder cable [10]. Other topologies that are discussed in the literature are, for example, the single- and double-sided ring topology and the star topology [10]. The main differences between the technologies are the redundancy of the systems and how this is handled in the best way with regard to costs and various technical considerations.

To the knowledge of the authors, there are no large-scale offshore wind farms with DC collection grids. However, DC collection grids have been considered for offshore wind power in many studies. Two types of main topologies can be identified in the literature: parallel and series collection grids [8], [10]–[15]. The main difference between the technologies is how the energy converters are connected to the grid, that is, electrically in parallel or in series.

Regardless of how the offshore grid is constructed the energy converters need to be connected to the grid. In AC offshore wind farms this is often achieved using a power electronic back-to-back (B2B) converter [7]. If a DC grid is considered the output from the generator needs to be rectified from AC to DC [16]. A simple solution is to use a passive rectifier. More advanced technologies with active rectifiers and possibly also DC/DC boosting steps can also be considered [16]. An active rectifier can make it possible to maximize power extraction. However, this will require more complicated components and control structures, which increases the complexity and possibly also the cost of the system.

The Division of Electricity at the Department of Electrical Engineering at Uppsala University has developed a vertical axis marine current energy converter [17]. The energy converter is deployed in the river Dalälven in Söderfors, Sweden. The turbine is five-bladed and placed on the riverbed. The generator is mounted on the same axis as the turbine without a gearbox. The electrical energy is transmitted to an onshore cabin via an approximately $150\,\mathrm{m}$ long cable [18]. In the onshore cabin, the electrical grid connection system is located. The grid connection system is based on a B2B converter technology [18], [19]. A simulation model of the system has been presented in [20].

Since the research in offshore power collection grids has mostly been focused on wind power, the study presented in this article considered low-voltage near-shore collection grids for the marine current energy converter technology at the Söderfors test site. One AC collection grid and one DC collection grid are simulated and compared with regards to stability and efficiency. The components and control schemes of the systems are presented and discussed. The AC and DC systems are also qualitatively compared for the marine current energy converter technology at the Söderfors test site.

II. Turbine and Generator

The turbine at the Söderfors test site is shown in Figure 1. A description of the test site and the turbine and the generator are given in [21] and [22]. A selection of turbine and generator parameters is given in Table 1. In this section, the turbine is first introduced and then the generator is briefly discussed.

A. Turbine

The turbine is an omnidirectional five bladed vertical axis turbine, as shown in Figure 1. A power coefficient, C_p, can be defined to describe the fraction of power the turbine can capture from the free-flowing water. The power coefficient is given by the following equation

$$C_p = \frac{P_{turbine}}{P_{water}}, \tag{1}$$

where $P_{turbine}$ is the power of the free-flowing water captured by the turbine and P_{water} is the power of the free-flowing water. The power of the turbine can be described by the power of a rotating body $P_{turbine} = \omega_t T_t$, where ω_t is the angular speed of the turbine and T_t is the torque.

The power of the free-flowing water is given by the following equation

$$P_{water} = \frac{1}{2} A \rho v_w^3, \tag{2}$$

where A is the area of the turbine, ρ is the density of the water and v_w is the velocity of the water.

The power coefficient is a function of the tip speed ratio, λ. The tip speed ratio is defined as the ratio between the tangential speed of the tip of the turbine blade and the velocity of the free-flowing water:

$$\lambda = \frac{\omega_t r}{v_w}, \tag{3}$$

where r is the radius of the turbine rotor.

The power coefficient can be described as a variable dependent on the tip speed ratio: $C_p(\lambda)$. The so called $C_p(\lambda)$-curve has been experimentally verified for the turbine in Söderfors in [23] for tip speed ratios from 2.9-4.5 in water flow velocities ranging from $1.2\,\mathrm{m/s}$ to $1.4\,\mathrm{m/s}$. A curve fitted from the experimental data is given by the following equation:

$$C_p(\lambda) = 0.0836\lambda^2 - 0.0183\lambda^3. \tag{4}$$

The experimentally fitted $C_p(\lambda)$-curve is shown in Figure 2. The optimal tip speed ratio calculated from the power coefficient curve is $\lambda_{opt} \approx 3.05$. This corresponds to an optimal power coefficient of $C_p(\lambda_{opt}) \approx 0.26$.

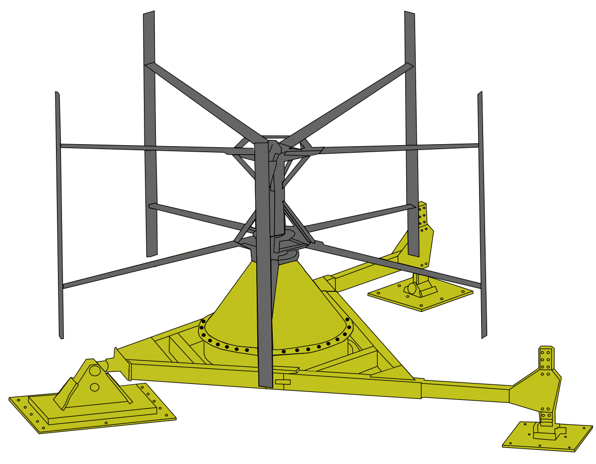

Fig. 1. The Marine current power unit with a vertical axis turbine and generator mounted on the same axis, placed on the riverbed. Reproduced with permission from [24].

B. Generator

The generator in the marine current energy converter at the experimental test site is a 112 pole, cable-wound non-salient permanent magnet synchronous generator (PMSG). The generator is rated at $7.5\,\mathrm{kW}$, $138\,\mathrm{V_{LL,rms}}$ at a nominal speed of $15\,\mathrm{rpm}$. The generator parameters are listed in Table I. The design and development of the generator are described in more detail in [25]. Additionally, in [26] it is shown that the efficiency of the generator is above $80\,\%$.

TABLE I
TURBINE AND GENERATOR PARAMETERS

Turbine	
$C_p(\lambda_{opt})$	0.26 at $\lambda_{opt} = 3.05$
Type	Vertical axis
Rotor height	3.5 m
Rotor radius (r)	3 m
Turbine area (A)	21 m^2
Generator	
Type	PMSG
Power rating	7.5 kW
Nominal rotational speed	15 rpm
Minimum efficiency	80 %
Number of poles	112
Rated voltage ($V_{LL,rms}$)	138 V
Rated stator current (rms)	31 A
Stator phase resistance	0.335 Ω
Armature inductance	3.5 mH
Flux linkage[b,c]	1.29 Wb
Inertia[c]	2445 kgm^2
Viscous friction coefficient[c]	1 Nms

[b] Assuming a constant flux.
[c] The values for flux linkage, inertia and viscous friction are estimates.

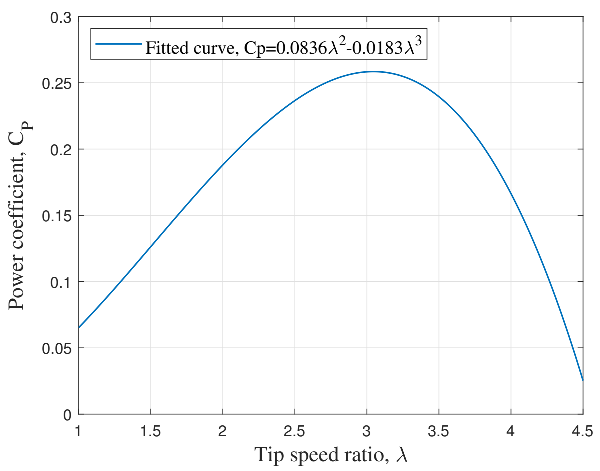

Fig. 2. Power coefficient (C_p) curve fitted from measurements [23]. Optimal tip speed ratio derived from the fitted curve is $\lambda_{opt} \approx 3.05$, which corresponds to an optimal power coefficient of $C_p(\lambda_{opt}) \approx 0.26$.

III. Electrical System

An overview of the electrical system at the Söderfors test site is shown in Figure 3. The system is extensively described in [18] and a comprehensive simulation study of the system can be found in [20]. An overview of the system will be given in this section.

The electrical system is based on a B2B converter technology, which is a common system in offshore wind power [7]. The system is bidirectional, which means that power can be transferred both to and from the generator. Usually, the direction of interest is from the generator to the external electrical grid. However, the turbine at the Söderfors test site is not self-starting [27]. The generator needs to be operated as a motor to achieve an angular velocity of the turbine high enough to start to rotate by itself. Therefore, the system needs to be bidirectional. However, for the study presented in this article, the focus is on the power transferred from the generator to the external grid. Considering this direction the electrical system can be summarized as follows. The turbine is used to convert the kinetic energy in the moving water to mechanical energy, which in turn is converted to electrical energy in the generator. The voltage output from the generator is in AC and is first rectified with a 2-level voltage source converter (2L-VSC). The power from the generator is before the 2L-VSC filtered with an LCL-filter formed by an LC-filter and the inductance of the generator. The 2L-VSC is connected to a 3-level VSC (3L-VSC) via a DC-link. The 3L-VSC inverts the DC voltage on the DC-link to AC voltages for the connection to the external AC grid. The AC output from the 3L-VSC is filtered with an LC-filter and the voltage is increased with a power transformer before the connection to the external electrical grid. The LC-filter together with the inductance of the power transformer constitutes an LCL-filter.

A benefit of a B2B converter is that the grid side and generator side of the system are effectively decoupled from each other [28]. This means that the two sides of the system can be controlled independently of each other. Therefore, the generator side and the grid side of the system will be treated separately below.

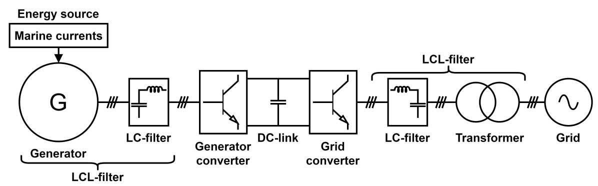

Fig. 3. Overview of the electrical system at the Söderfors test site.

A. *DC grid side – generator side*

In Figure 4, the generator side of the electrical system is shown in more detail. This part of the system encompasses the generator, the LC-filter and the 2L-VSC. The AC output from the generator is rectified by the 2L-VSC. In the study presented in this paper the generator side of the electrical system is used in two ways: 1) as one part of a B2B converter in order to generate a DC output for the DC-link (see Figure 3), and 2) to generate a DC voltage for the connection of a turbine to a DC collection grid. In both cases the same control scheme is used, shown in Figure 4 and further discussed below. The control of the generator side in the context of the specific B2B converter has been comprehensively evaluated in [20].

The control of the generator side VSC is aimed at achieving optimal power extraction from the turbine. This is achieved with a field-oriented control (FOC) algorithm together with a maximum power point tracking (MPPT) scheme. In the FOC method, the phase currents from the generator are transformed into a rotating reference system using a dq-transform. The

TABLE II
ELECTRICAL SYSTEM PARAMETERS

Component	Parameters	Values
Cable	Resistance	$0.524\,\Omega/\mathrm{km}$
	Inductance	$0.24\,\mathrm{mH/km}$
Rectifier	Converter type	2L-VSC
	Modulation scheme	SPWM
	Switching frequency	4 kHz
	Harmonic LC filter	1.6 mH, 10 μF
DC-link filter	Capacitor bank	16.5 mF
Inverter	Converter type	3L-VSC
	Modulation scheme	SPWM
	Switching frequency	6 kHz
	Harmonic LC filter	2.4 mH (66 mΩ)
		10 μF
	Damping resistance	2.31 Ω
Transformer	Delta/Wye	400 V/230 V
	Power rating	7.5 kVA
	Primary resistance	0.7 Ω
	Secondary resistance	0.23 Ω
	Primary leak. inductance	0.9 mH
	Seconday leak. inductance	0.3 mH
	Magnetization resistance	8225 Ω
	Magnetization inductance	9.22 H
Grid	Three-phase symetrical	400 V/50 Hz
IGBT	Internal resistance	0.1 mΩ
	Forward voltage	1 V
Rectifier diode	Internal resistance	0.001 Ω
	Forward voltage	0.8 V
Snubber circuit	Snubber resistance	47 kΩ
	Snubber capacitance	470 nF

generator is then controlled using the dq currents i_{ds} and i_{qs}. The specific method used here is zero d-axis current control, where the d-axis current is maintained at zero, $i_{ds} = 0$. In this case, the stator current of the generator becomes equal to the q-axis current, i_{qs}, and it can be shown that the electromagnetic torque is given by the following equation:

$$T_e = \frac{3}{2} p \psi_r i_{qs}, \tag{5}$$

where p is the number of pole pairs and ψ_r is the rotor flux linkage. If the rotor flux linkage is assumed to be constant the relationship between the electromagnetic torque and the q-axis current is linear. Consequently, by controlling the q-axis current it is possible to control the electromagnetic torque, and by changing the electromagnetic torque it is possible to regulate the angular speed of the turbine.

In order to decide a suitable reference value for the q-axis current the MPPT scheme is used. The aim of the implemented MPPT scheme is to adjust the angular speed of the turbine in order to achieve optimal tip speed ratio, $\lambda_{opt} \approx 3.05$, for a specific water speed. The implemented MPPT scheme is shown in Figure 4. Input parameters to the MPPT block are the water speed, v_w, and the angular speed of the turbine, ω_t. The optimal tip speed ratio, λ_{opt}, and the water speed is used with Equation 3 to calculate a reference value for the angular speed of the turbine, $\omega_{t,ref}$. The reference value is compared with the actual rotational speed of the turbine (in this article the electrical angular speed was used) and the error is sent to a PI controller. The output from the PI controller, which is also the output from the MPPT block, is the reference value for the q-axis current, i^*_{qs}.

The other parts of the implemented FOC control strategy are as follows. The outer control loop is constituted by the PI regulator in the MPPT block. Additionally, two inner control loops with two PI regulators for the control of the dq-axis currents are used, as shown in Figure 4. However, in order to control the dq-currents, the phase currents from the generator need to be transformed into dq-currents. This is achieved by measuring the angular speed of the turbine and using an integrator to generate the electrical angle of the turbine, θ_e, which is used to create the rotating reference frame. The phase currents are measured and together with the electrical angle the dq currents of the generator are produced in the block abc/dq. The output from the MPPT block, i^*_{qs}, is compared with the measured q-axis current. The error is sent to one of the inner loop PI controllers, which generates reference values for q-axis voltage, v^*_{qs}. The measured value of the d-axis current is compared with the reference value $i^*_{ds} = 0$, and the error is sent to the other PI regulator, which generates the reference voltage v^*_{ds}. The reference dq-voltages are transformed back to the stationary reference frame and used as reference signals in a pulse-width modulation (PWM) block, which generates control signals for the 2L-VSC converter using a sinusoidal carrier-based PWM (SPWM) technique.

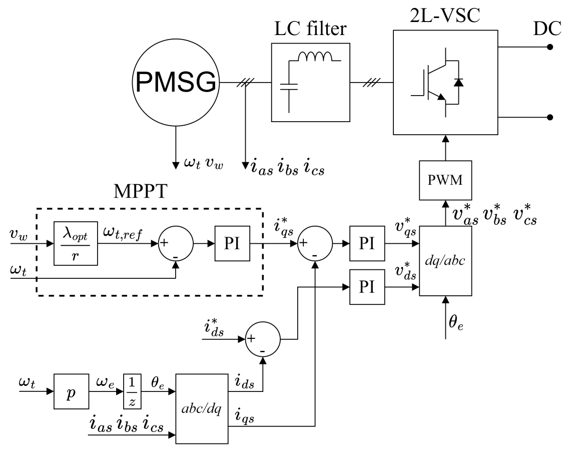

Fig. 4. Generator side of the B2B converter. Main components and control scheme.

B. AC grid side – external electrical grid

The part of the electrical system connected to the AC grid, shown in Figure 3, is considered in two ways in this paper: 1) as the AC side of a conventional B2B converter, as in Figure 3, and 2) the AC side for multiple turbines in a DC collection grid. The same control method is used in both cases. The purpose of the AC side of the system is to invert the DC voltage on the DC-link (or DC collection grid) to AC voltage, in order to connect the system to the external distribution grid. The external grid is assumed to be strong. The aim of the implemented control is to take the power that enters the DC side and inject the power into the AC grid while maintaining the voltage level on the DC side. This is achieved using a voltage oriented control (VOC) with a phase-locked loop (PLL) scheme, shown in Figure 5. The PLL algorithm is used to detect the grid voltage angle, θ_g, which is used for the transformation of voltages and currents from a stationary to a rotating reference system.

The VOC control scheme requires that the d-axis of the rotating coordinate system is aligned with the grid voltage vector. The magnitude of the d-axis component will in this case be equal to the magnitude of the grid voltage vector [28]. When this is the case, the q-axis voltage will be zero, and it can be shown that the active and reactive power exchanged with the grid are given by the following equations in the dq reference frame:

$$P_g = \frac{3}{2}(v_{dg}i_{dg} + v_{qg}i_{qg}) = \frac{3}{2}v_{dg}i_{dg}, \tag{6}$$

$$Q_g = \frac{3}{2}(v_{qg}i_{dg} - v_{dg}i_{qg}) = -\frac{3}{2}v_{dg}i_{qg}. \tag{7}$$

Equation 7 can be re-written to give an expression for the reference value for the q-axis current:

$$i^*_{qg} = \frac{Q^*_g}{-1.5v_{dg}}, \tag{8}$$

where Q^*_g is reference value for the reactive power and v_{dg} is the d-component of the grid side voltages. Equation 8 can be used to control the reactive power exchanged with the grid and if $Q^*_g = 0$, unity power factor is achieved.

It is customary to disregard the filter capacitor when designing the controller for a grid-connected VSC with an LCL-filter. It can be shown that the state equations for the AC side of a grid-connected VSC with an L-filter are given by the following system of equations [28]:

$$\begin{aligned} L\frac{di_{dg}}{dt} &= (v_{dg} - v_{di} + \omega_g L i_{qg}) \\ L\frac{di_{qg}}{dt} &= (v_{qg} - v_{qi} - \omega_g L i_{dg}) \end{aligned} \tag{9}$$

where v_{di} and v_{qi} are the dq-components of the converter phase voltages and ω_g is the angular frequency of the grid. The d- and q-axis components are coupled by the terms $\omega_g L i_{dg}$ and $\omega_g L i_{qg}$. In order to simplify the design of the PI controllers it is common to decouple the dq-components from each other when implementing the controller [28]. In Figure 5, this is performed in the block "Decoupled controller".

The VOC scheme shown in Figure 5 is based on two inner control loops for the control of the dq-axis currents and one outer control loop for the control of the DC-link voltage. The outer control loop uses one PI regulator to produce a reference value for the grid side d-axis current, i^*_{dq}. The inner control loops, implemented with two PI controllers, generate reference dq-voltages for the VSC, which are transformed into a stationary coordinate system and used as reference signals in the PWM block in order to generate control pulses for the VSC. The PWM block uses a sinusoidal carrier-based PWM method to generate the control pulses.

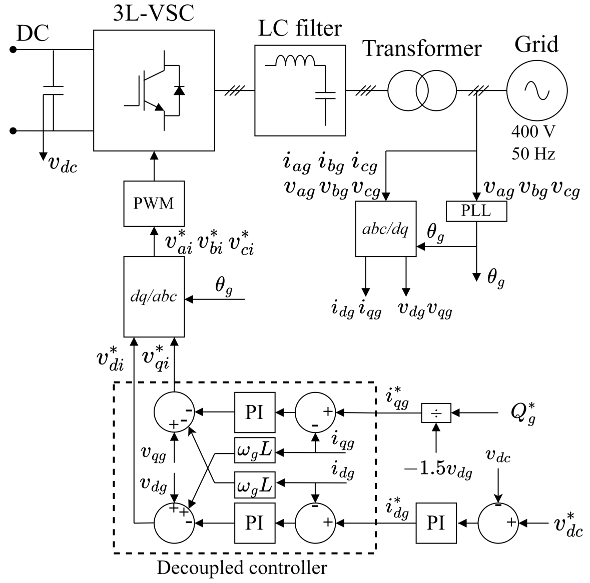

Fig. 5. Grid side of the B2B converter. Main components and control scheme.

C. Resonance of the AC grid side LCL-filter

An LCL-filter has a high-frequency attenuation rate of $-60\,\mathrm{dB}$, which can be compared with $-20\,\mathrm{dB}$ for an L-filter and $-40\,\mathrm{dB}$ for an LC-filter [29]. The significant high-frequency attenuation rate together with the fact that smaller components can be used has made the LCL-filter the preferred choice when designing filters for grid-connected VSC [30]. The LCL-filter is, however, associated with a resonance peak at a certain frequency. The resonance peak in the frequency response of the LCL-filter can adversely affect the control of a VSC [31]. In order to limit the effect of the resonance peak on the controller a resonance damping strategy can be used. There are two methods to dampen a resonance peak: passive and active damping [31]. Passive damping techniques are based on the inclusion of passive components, for example, a resistor in the system in order to decrease the resonance peak. The active damping techniques are based on the modification of the control strategy of the VSC to achieve a virtual damping of the resonance peak.

The transfer function of the LCL-filter is commonly used to analyse the resonance behaviour of the filter. In the system considered in this paper, the AC grid side LCL-filter is formed by an LC-filter and the inductance of a power transformer. If the LC-filter and power transformer are assumed to be lossless and the core components of the transformer are disregarded, the transfer function from the AC voltage output of the grid side VSC to the grid current can be derived to the following equation:

$$H_{LCL} = \frac{1}{n} \cdot \frac{1}{L_f C_f (L_s + L'_p)s^3 + (L_f + L_s + L'_p)s}, \tag{10}$$

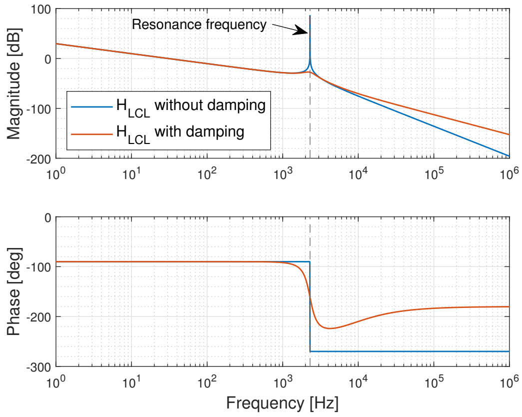

Fig. 6. Frequency response of the grid side LCL-filter without and with passive damping.

where L_f and C_f are the filter inductance and capacitance, respectively. L_s is the secondary side leakage inductance of the transformer, L'_p is the primary side leakage inductance of the transformer referred to the secondary side of the transformer, and n is the turns ratio of the transformer. The resonance frequency of the system can be calculated with the following equation:

$$\omega_{res} = \sqrt{\frac{L_f + L_s + L'_p}{L_f C_f (L_s + L'_p)}}. \tag{11}$$

The Bode plot of the transfer function in Equation 10 is shown in Figure 6. The resonance peak is clearly visible in the magnitude and from Equation 11 and the parameter values in Table II the resonance frequency can be calculated to 2300 Hz.

In order to stabilize the grid side controller a passive damping strategy is used, where resistors are placed in series with the filter capacitors. A suitable value for the damping resistance can be calculated with the following equation [32]:

$$R_d = \frac{1}{3\omega_{res} C_f} \tag{12}$$

For the resonance frequency of 2300 Hz and the filter capacitor value from Table II, the damping resistance is calculated to 2.31 Ω. Figure 6 shows the frequency response after the addition of the series resistances, and it is clearly visible that the resonance peak is significantly attenuated.

IV. Power Collection Grids

Two types of near-shore low-voltage power collection grids are considered in this study: one conventional AC collection grid and one DC collection grid. Both grids consist of five marine current energy converters. The first converter is located 200 m from the shoreline. The other four energy converters are respectively spaced three times the diameter (3D) of the turbines from each other, starting from the first turbine. This corresponds to 18 m between each turbine. The same cable is assumed for both cases with the per meter parameter values as in Table II. A simplified lumped element model of the cable is used where only the series resistance and series inductance are considered.

A. AC collection grid

The AC collection grid is shown in Figure 7. Five turbines are connected to a radial three-phase feeder cable, which on the land is connected to the point of common coupling (PCC). The electrical system of the turbines is the system shown in Figure 3. This includes the filters, the B2B converter and the transformer. It is assumed that all the components of the system are contained in the turbine or placed in the immediate closeness to the turbine at sea. In Figure 7, the turbine with the electrical system is illustrated by the dotted box.

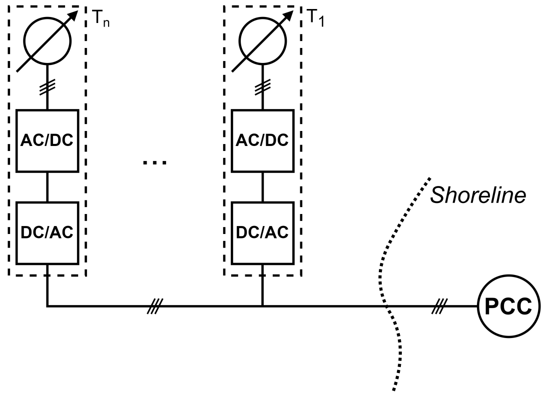

Fig. 7. Radial AC collection grid with 5 turbines connected to the shore via a 200 m AC cable

B. DC collection grid

In Figure 8, the DC collection grid is shown. The turbines are connected electrically in parallel to the grid. The turbine with the electrical system is illustrated by the dotted box. The electrical system now only encompasses the generator side of the system shown in Figure 3. Additionally, a capacitor with the capacitance value 16.5 mF is placed at the DC-side of the VSC at all turbines. The power is transmitted to the shore by the DC collection grid. On the shore, the AC grid side of the system shown in Figure 3 is used to inject the power into the distribution grid. A capacitor with the value 16.5 mF is placed on the DC side of the grid side VSC in order to stabilize the voltage on the DC collection grid.

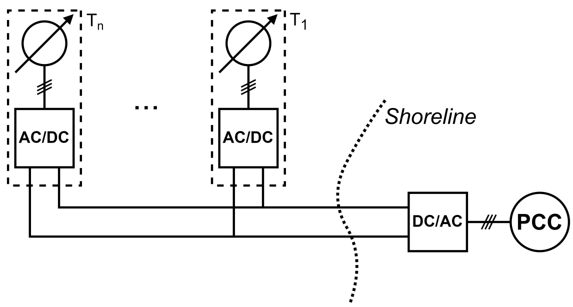

Fig. 8. Parallel DC collection grid with 5 turbines connected to the shore via a 200 m DC cable.

V. Simulation model

The collection grids are implemented in MATLAB/Simulink using built-in functions and building blocks. The turbine is modelled using the $C_p(\lambda)$-curve in Equation 4, which is used together with the water speed to calculate the torque on the generator. The input variable to the models is different water speeds. The parameters in the models are from Table I and II. The resistances and inductances of the cables are from Section IV.

The PI controllers are implemented as discrete-time parallel controllers.

The models are simulated in discrete time. The electrical components are sampled at a time step of $1\,\mu$s. The other components in the model, for example, the PI controllers, are sampled at a time step determined automatically by Simulink. The solver is a variable-step solver automatically determined by Simulink.

VI. Simulation results and discussion

In this section, the collection grids are evaluated with an emphasis on the results from simulations.

A. Steady-state simulations

The AC and DC systems are simulated with constant water speeds applied to all turbines. The water speeds are close to the nominal value for the turbine, $1.35\,\mathrm{m/s}$. The water speeds differ a bit between the turbines in order to evaluate the performance of the systems when different water speeds are applied to the turbines. The water speeds are the following: $v_{w,\mathrm{T}_1} = 1.30\,\mathrm{m/s}$, $v_{w,\mathrm{T}_2} = 1.35\,\mathrm{m/s}$, $v_{w,\mathrm{T}_3} = 1.33\,\mathrm{m/s}$, $v_{w,\mathrm{T}_4} = 1.28\,\mathrm{m/s}$ and $v_{w,\mathrm{T}_5} = 1.34\,\mathrm{m/s}$.

1) AC collection grid: The voltages of the AC collection grid are determined by the strong grid. Therefore, the currents are of most interest to evaluate the performance of the controllers. In Figure 9, the AC current for one phase is shown at six points of the AC collection grid: at the connection point to the distribution grid (the PCC in Figure 7) and at the connection points to the five turbines. The currents are shown for a time interval of $0.2\,$s, when the system operates in steady-state. In accordance with Kirchhoff's current law, the current injected into the distribution grid ($i_{a,grid}$) is the sum of the five currents from the turbines. As can be observed the current injected into the distribution grid and the currents from the turbines are stable sinusoidal waveforms.

The purpose of the control system is to make the system inject the power from the turbines into the distribution grid. In Figure 10, the mechanical power to the turbines ($P_{gen,tot}$), the electrical power from the turbines ($P_{turbines,tot}$) and the total power injected into the grid at the PCC ($P_{AC,grid}$) are shown. Initially, before the system settles into steady-state, there are some transients. However, the system stabilizes in less than $1.5\,$s. At steady-state operation, there is a difference in power levels in the different parts of the system, which is due to resistive losses. The control system in the turbines works as expected, in that the power from the turbines is delivered to the PCC. The tip speed

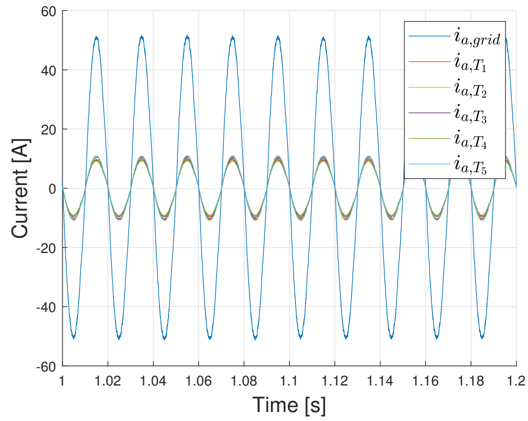

Fig. 9. Steady-state AC currents, phase a.

ratio is calculated using Equation 3 and it is verified that all turbines operate at the optimal tip speed ratio, $\lambda_{opt} = 3.05$.

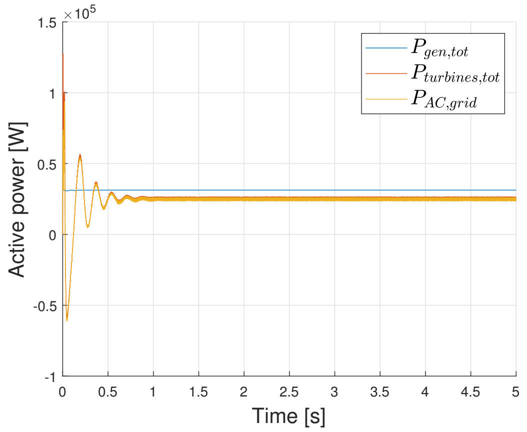

Fig. 10. Steady-state power levels for the AC collection grid.

2) DC collection grid: The AC grid side controller should in the DC system be able to maintain the DC voltage level of the collection grid at a specific value. The reference value for the DC voltage is $400\,$V. The voltage of the collection grid is regulated with regard to the DC voltage level at the AC grid side inverter. The simulated DC voltages at the turbines and the grid side inverter are shown in Figure 11. When the simulation is started there are some initial transients before the system settles to a steady-state at around $1.5\,$s. After the transients, it can be observed the voltage level at the grid side inverter, $v_{DC,grid}$, is maintained at $400\,$V while the voltage levels at the turbines are higher than the reference value. This is explained by the resistance of the cables. Since the cables are modelled by a series resistance and inductance and a current is present in the cables, a voltage droop needs to occur over the cable segments. This will force the DC voltages to higher levels at the turbines compared to the DC voltage level at the AC grid side inverter.

The power flow in different parts of the DC system is shown in Figure 12. Again some initial transients can be observed. The blue curve, $P_{gen,tot}$, is the total mechanical power to the generators. The total power in-

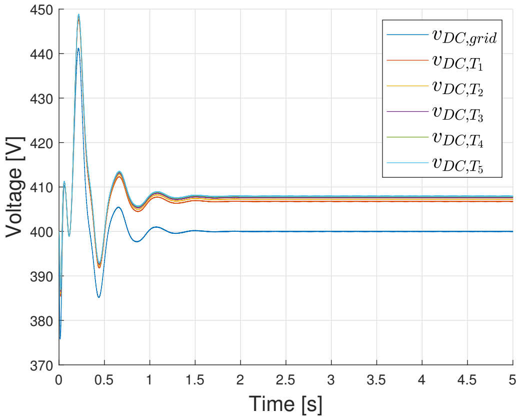

Fig. 11. Steady-state DC voltages.

jected into the DC grid from the turbines is represented by the red curve, $P_{turbines,tot}$. The difference between these curves is the conduction losses in the turbines, which encompasses the losses in the generators and the 2L-VSCs. The yellow curve, $P_{DC,grid}$, is the power on the DC-side of the AC grid side inverter. The difference between these curves is the conduction losses in the DC collection grid. The active power injected into the AC distribution grid is given by the purple curve, $P_{AC,grid}$, and as can be observed there are some conduction losses in the 3L-VSC and the power transformer. Finally, the reactive power exchanged with the AC grid is given by the green curve, $Q_{AC,grid}$. The reference value for the reactive power is set to zero. The mean value of the reactive power in Figure 12 is calculated to be zero.

The tip speed ratios are calculated using Equation 3 and confirmed to be at the optimal value for all turbines. Consequently, it can be concluded that the system has the desired function, in that, the turbines operate at optimal tip speed ratio and the power from the turbines is transmitted via the DC collection grid to the onshore converter and injected into the AC distribution grid. Be that with some conduction losses, which are further discussed in Section VI-B.

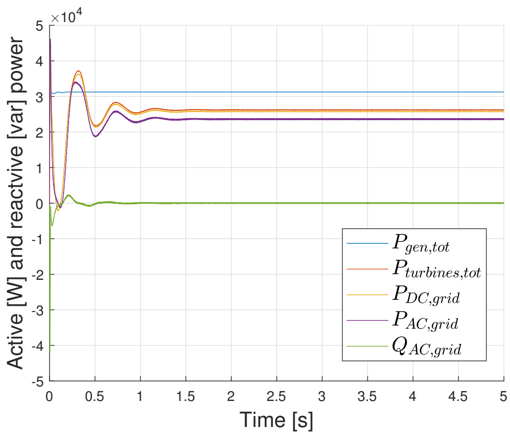

Fig. 12. Steady-state power levels for the DC collection grid.

B. *Power losses in the AC and DC systems*

The simulation models are used to evaluate the power losses in the AC and DC systems for three water speed cases:

1) nominal water speeds ($v_{w,\mathrm{T}_1} = 1.30\,\mathrm{m/s}$, $v_{w,\mathrm{T}_2} = 1.35\,\mathrm{m/s}$, $v_{w,\mathrm{T}_3} = 1.33\,\mathrm{m/s}$, $v_{w,\mathrm{T}_4} = 1.28\,\mathrm{m/s}$ and $v_{w,\mathrm{T}_5} = 1.34\,\mathrm{m/s}$),
2) low water speeds ($v_{w,\mathrm{T}_1} = 0.85\,\mathrm{m/s}$, $v_{w,\mathrm{T}_2} = 0.9\,\mathrm{m/s}$, $v_{w,\mathrm{T}_3} = 0.93\,\mathrm{m/s}$, $v_{w,\mathrm{T}_4} = 0.88\,\mathrm{m/s}$ and $v_{w,\mathrm{T}_5} = 0.91\,\mathrm{m/s}$), and
3) high water speeds ($v_{w,\mathrm{T}_1} = 1.65\,\mathrm{m/s}$, $v_{w,\mathrm{T}_2} = 1.6\,\mathrm{m/s}$, $v_{w,\mathrm{T}_3} = 1.58\,\mathrm{m/s}$, $v_{w,\mathrm{T}_4} = 1.61\,\mathrm{m/s}$ and $v_{w,\mathrm{T}_5} = 1.57\,\mathrm{m/s}$).

The losses for the DC system are evaluated for three different voltage levels for each water speed case: $400\,\mathrm{V}$, $600\,\mathrm{V}$ and $1000\,\mathrm{V}$. The power losses only include conduction losses, that is, the switching losses of the VSCs are not included.

The results from the simulations are shown in Table III, where the losses of the DC systems are expressed relative to the losses of the AC system. This means that if the factor in the table has the value 1 ("one") then the losses are the same in the AC and DC systems. If the value is less than one, then the losses in the DC system are less than the losses in the AC system, and vice versa. The column $P_{rel,loss,grid}$ is the conduction losses in the collection grid cables. In the last column, the total losses of the system are given.

For all three cases, the losses in the DC collection grid cables decrease when the voltage is increased. This is expected because the current decreases when the voltage is increased for a given power level. Furthermore, it should be noted that the total losses for nominal and high water speeds are higher in the DC collection grid. However, for low water speeds, the losses are lower for the DC system at the voltage levels $400\,\mathrm{V}$ and $600\,\mathrm{V}$.

TABLE III
THE POWER LOSSES IN THE DC COLLECTION GRID RELATIVE TO THE POWER LOSSES IN THE AC COLLECTION GRID.

Case 1 – nominal water speeds		
Voltage level	$P_{rel,loss,grid}$	$P_{rel,loss,tot}$
$400\,\mathrm{V_{DC}}$	1.08	1.18
$600\,\mathrm{V_{DC}}$	0.49	1.15
$1000\,\mathrm{V_{DC}}$	0.18	1.15
Case 2 – low water speeds		
Voltage level	$P_{rel,loss,grid}$	$P_{rel,loss,tot}$
$400\,\mathrm{V_{DC}}$	1.12	0.92
$600\,\mathrm{V_{DC}}$	0.5	0.94
$1000\,\mathrm{V_{DC}}$	0.17	1.03
Case 3 – high water speeds		
Voltage level	$P_{rel,loss,grid}$	$P_{rel,loss,tot}$
$400\,\mathrm{V_{DC}}$	0.99	1.20
$600\,\mathrm{V_{DC}}$	0.40	1.20
$1000\,\mathrm{V_{DC}}$	0.16	1.20

C. *Disconnection of a turbine*

The stability of the systems is evaluated by disconnecting turbine 3 (T_3) when the system is operating in steady-state. A simulation is started and the system is allowed to settle into steady-state. An ideal breaker is then used at $2.5\,\mathrm{s}$ to disconnect turbine 3 from the AC and DC collection grids, respectively.

1) AC collection grid: In Figure 13, the phase a currents are shown at the instance of the disconnection of turbine 3. As can be observed, the loss of turbine 3 has no noticeable impact on the currents from the other turbines. The current injected into the distribution grid ($i_{a,grid}$) is also stable.

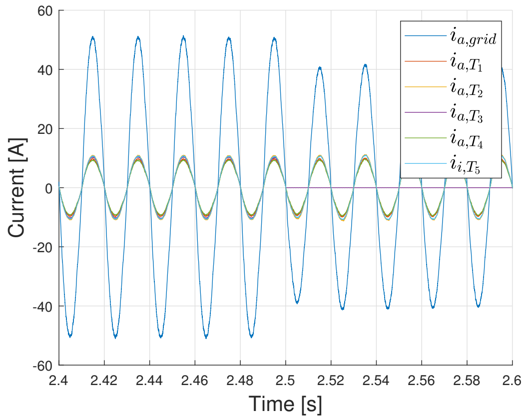

Fig. 13. Currents, phase a, in the AC collection grid at a sudden disconnection of turbine 3 (T_3) at 2.5 s.

Figure 14 shows the power from the turbines and the power injected into the distribution grid at the PCC. As can be observed, a transient appears in the power from the turbines when turbine 3 is disconnected. This is due to a transient in the voltage that occurs when the breaker is opened. However, the power from the turbines stabilizes very quickly after the disconnection. The turbines that are still connected to the grid are able to deliver power to the grid at the optimal tip speed ratio. However, since one turbine is disconnected, the power injected into the distribution grid is at a lower level.

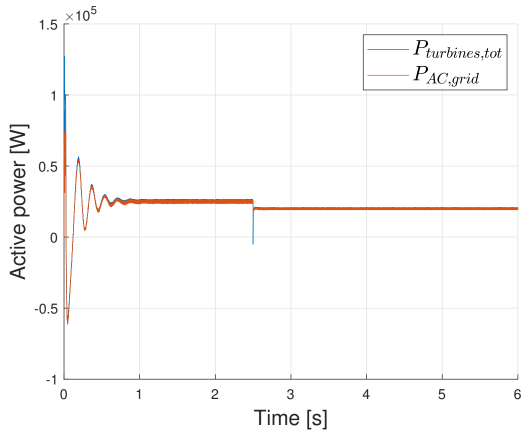

Fig. 14. Power in the AC collection grid at a sudden disconnection of turbine 3 (T_3) at 2.5 s.

2) DC collection grid: In Figure 15, the voltage levels on the DC collection grid are shown. As can be observed a transient occurs in the voltage at turbine 3 at 2.5 s. The system is stabilized within one second of the disconnection of turbine 3. In Figure 16, the power at different parts of the system is shown. As can be seen, the power from the turbines is decreased when one turbine is lost. However, the power from the turbines and the power injected into the AC grid are able to find a new equilibrium quickly. The reactive power exchanged with the external distribution grid is maintained at zero, only with a small disturbance when the turbine is disconnected.

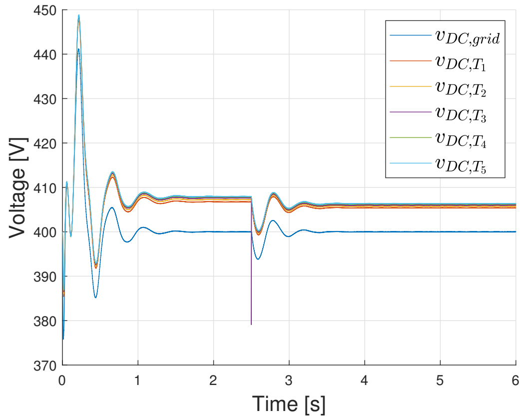

Fig. 15. Voltages in the DC collection grid at a sudden disconnection of turbine 3 (T_3) at 2.5 s.

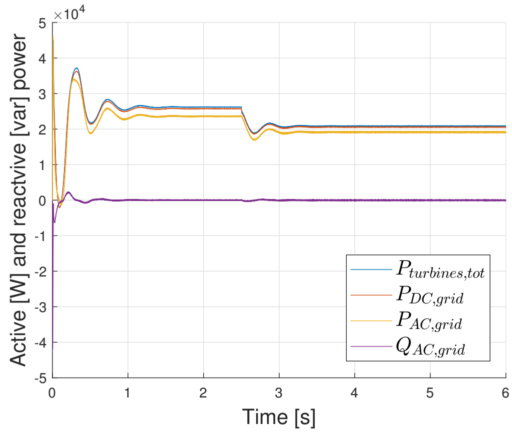

Fig. 16. Power in the DC collection grid at a sudden disconnection of turbine 3 (T_3) at 2.5 s.

D. A qualitative discussion of AC and DC collection grids for marine current power

Both the AC and DC collection grids are able to transmit the power to the shore and inject the power into the distribution grid. The simulations have shown that both systems are stable with regard to a disturbance, that is, the disconnection of one turbine. The total power losses of the AC system are lower than those of the DC system for nominal and high water speeds. For low water speeds the total power losses are lower for the DC system, when the voltage is 400 V and 600 V. However, it should be observed that the power losses shown in Table III did not include switching losses. Since the AC system requires five VSC instead of one as in the DC system, the switching losses can be expected to be significantly higher for the AC system compared with the DC system.

In both systems, all components were assumed to be placed in the turbine (or very close to the turbine).

The main advantage of the AC system is that it is based on established technologies from the offshore wind power sector. However, since space limitations and maintenance difficulties are constraining factors in offshore engineering, it can be beneficial to consider a system that requires fewer components to be placed in the turbine. The DC collection grid considered in this study only requires a rectifier in the turbine compared with a full B2B converter system as in the discussed AC collection grid. Additionally, even though the power losses were larger in the DC grid they were not radically higher and if the switching losses were to be included, the difference between the two systems would be expected to decrease. These factors, in addition to the fact that fewer cables are needed in the DC system (only one cable if the sea is used as a return conductor), make the DC system an interesting option.

VII. Summary and conclusions

A simulation study of AC and DC collection grids for a marine current energy converter has been presented. It has been shown that the proposed control algorithms can be used to correctly control the turbines and inject the power from the turbines into the distribution grid. The control is stable for both the AC and DC systems, even when a turbine is suddenly disconnected from the grid. The AC collection grid has lower total power losses for nominal and high water speeds. However, the difference in losses between the systems is within a $20\,\%$ range. Considering the fact that fewer components need to be placed in the turbine in the DC collection grid compared with the AC collection grid and that fewer cables are needed, the DC system could be an interesting option.

Acknowledgement

The work was supported by STandUP for Energy.

References

[1] "Renewables 2022 Global Status Report," REN21 Secretariat, Tech. Rep., Paris, France, 2022.

[2] "Marine Energy Electrical Architecture - Report 1: Landscape Map and Literature Review," CATAPULT Offshore Renewable Energy (CORE), Tech. Rep., September 2015.

[3] "Marine Energy Electrical Architecture - Report 2: Review of SSE Contractor Reports ," CATAPULT Offshore Renewable Energy (CORE), Tech. Rep., September 2015.

[4] "Marine Energy Electrical Architecture - Report 3: Optimum Electrical Array Architectures," CATAPULT Offshore Renewable Energy (CORE), Tech. Rep., September 2015.

[5] A. J. Collin, A. J. Nambiar, D. Bould, B. Whitby, M. A. Moonem, B. Schenkman, S. Atcitty, P. Chainho, and A. E. Kiprakis, "Electrical components for marine renewable energy arrays: A techno-economic review," *Energies*, vol. 10, no. 12, 2017.

[6] Z. Li, Q. Song, F. An, B. Zhao, Z. Yu, and R. Zeng, "Review on DC transmission systems for integrating large-scale offshore wind farms," *Energy Conversion and Economics*, vol. 2, no. 1, pp. 1–14, Feb. 2021.

[7] F. Blaabjerg and K. Ma, "Wind energy systems," *Proceedings of the IEEE*, vol. 105, no. 11, pp. 2116–2131, Nov. 2017.

[8] R. Srikakulapu and U. Vinatha, "Electrical collector topologies for offshore wind power plants: A survey," in *Proc. 2015 IEEE 10th International Conference on Industrial and Information Systems (ICIIS)*, Peradeniya, Sri Lanka, Dec. 18-20, 2015, pp. 338–343.

[9] G. Quinonez-Varela, G. W. Ault, O. Anaya-Lara, and J. R. McDonald, "Electrical collector system options for large offshore wind farms," *IET Renewable Power Generation*, vol. 1, no. 2, pp. 107–114, Jun. 2007.

[10] S. Lumbreras and A. Ramos, "Offshore wind farm electrical design: a review," *Wind Energy*, vol. 16, no. 3, pp. 459–473, Apr. 2013.

[11] S. M. Alagab, S. Tennakoon, and C. Gould, "Review of wind farm power collection schemes," in *Proc. 2015 50th International Universities Power Engineering Conference (UPEC)*, Stoke on Trent, UK, Sep. 1-4, 2015.

[12] H. J. Bahirat, B. A. Mork, and H. K. Høidalen, "Comparison of wind farm topologies for offshore applications," in *Proc. 2012 IEEE Power and Energy Society General Meeting*, San Diego, CA, USA, Jul. 22-26, 2012.

[13] P. Lakshmanan, R. Sun, and J. Liang, "Electrical collection systems for offshore wind farms: A review," *CSEE Journal of Power and Energy Systems*, vol. 7, no. 5, pp. 1078–1092, Sep. 2021.

[14] S. Lundberg, "Wind farm configuration and energy efficiency studies: series DC versus AC layouts," Ph.D. dissertation, Chalmers University of Technology, 2006.

[15] S. Lundberg, "Evaluation of wind farm layouts," *EPE Journal (European Power Electronics and Drives Journal)*, vol. 16, no. 1, pp. 14–21, Feb. 2006.

[16] C. G. Dincan, "High power medium voltage DC/DC converter technology for DC wind turbines," Ph.D. dissertation, Aalborg University, 2018.

[17] S. Lundin, J. Forslund, N. Carpman, M. Grabbe, K. Yuen, S. Apelfröjd, A. Goude, and M. Leijon, "The Söderfors project: Experimental hydrokinetic power station deployment and first results," in *Proc. 10th European Wave and Tidal Energy Conference (EWTEC)*, Aalborg, Denmark, Sep. 2-5, 2013.

[18] S. Apelfröjd, R. Ekström, K. Thomas, and M. Leijon, "A back-to-back 2l-3l grid integration of a marine current energy converter," *Energies*, vol. 8, pp. 808–820, 2015.

[19] S. Apelfröjd, "Grid connection of permanent magnet generator based renewable energy systems," Ph.D. dissertation, Uppsala University, 2016.

[20] C. Fjellstedt, J. Forslund, and K. Thomas, "Simulations of the electrical system of a grid connected marine current energy converter," in *Proc. Fourteenth European Wave and Tidal Energy Conference*, Plymouth, UK, Sep. 5-9, 2021.

[21] M. Grabbe, K. Yuen, A. Goude, E. Lalander, and M. Leijon, "Design of an experimental setup for hydro-kinetic energy conversion," *International Journal on Hydropower & Dams*, vol. 16, no. 5, pp. 112–106, 2009.

[22] K. Yuen, S. Lundin, M. Grabbe, E. Lalander, A. Goude, and M. Leijon, "The Söderfors Project: Construction of an Experimental Hydrokinetic Power Station," in *Proc. Ninth European Wave and Tidal Energy Conference*, Southampton, UK, Sep. 5-9, 2011.

[23] S. Lundin, J. Forslund, A. Goude, M. Grabbe, K. Yuen, and M. Leijon, "Experimental demonstration of performance of a vertical axis marine current turbine in a river," *Journal of Renewable and Sustainable Energy*, vol. 8, no. 6, pp. 112–106, 2016, Art. no. 064501.

[24] J. Forslund, "Studies of a vertical axis turbine for marine current energy conversion: Electrical system and turbine performance," Ph.D. dissertation, Uppsala University, 2018.

[25] M. Grabbe, "Hydro-kinetic energy conversion: Resource and technology," Ph.D. dissertation, Uppsala University, 2013.

[26] M. Grabbe, K. Yuen, S. Apelfröjd, and M. Leijon, "Efficiency of a directly driven generator for hydrokinetic energy conversion," *Advances in Mechanical Engineering*, 2013, Art. no. 978140.

[27] J. Forslund, K. Thomas, and M. Leijon, "Power and energy needed for starting a vertical axis marine current turbine," in *Proc. 12th European Wave and Tidal Energy Conference (EWTEC)*, Cork, Ireland, Aug. 27 - Sep. 1, 2017.

[28] B. Wu, Y. Lang, N. Zargari, and S. Kouro, *Power conversion and control of wind energy systems*, 1st ed. Hoboken, New Jersey, US: John Wiley & Sons, 2011.

[29] Y. Han, M. Yang, H. Li, P. Yang, L. Xu, E. A. A. Coelho, and J. M. Guerrero, "Modeling and stability analysis of LCL-type grid-connected inverters: A comprehensive overview," *IEEE Access*, vol. 7, pp. 114 975–115 001, Aug. 2019.

[30] S. Jayalath and M. Hanif, "Generalized LCL-filter design algorithm for grid-connected voltage-source inverter," *IEEE Transactions on Industrial Electronics*, vol. 64, no. 3, pp. 1905–1915, 2017.

[31] C. C. Gomes, A. F. Cupertino, and H. A. Pereira, "Damping techniques for grid-connected voltage source converters based on LCL filter: An overview," *Renewable and Sustainable Energy Reviews*, vol. 81, pp. 116–135, Jan. 2018.

[32] S. V. Araujo, A. Engler, B. Sahan, and F. L. M. Antunes, "LCL filter design for grid-connected NPC inverters in offshore wind turbines," in *Proc. 2007 7th International Conference on Power Electronics*, 2007, pp. 1133–1138.